Title

Magnetic state switching in FeGa microstructures

Journal

Smart Materials and Structures, 31(3)

ISSN

0964-1726

Authors

De Jesus, Michael Guevara

Xiao, Zhuyun

Goiriena-Goikoetxea, Maite

et al.

Publication Date

2022-03-01

DOI

10.1088/1361-665x/ac46db

Magnetic State Switching in FeGa Microstructures

Michael Guevara De Jesus[1], Zhuyun Xiao[2], Maite Goiriena-Goikoetxea[3,4], Rajesh V. Chopdekar[5], Mohanchandra K. Panduranga[1], Paymon Shirazi[1], Adrian Acosta[6], Jane P. Chang[6], Jeffrey Bokor[3], Gregory P. Carman[1], Rob N. Candler[2,7], and Christopher Lynch[1,8*]

[1]Department of Mechanical and Aerospace Engineering, University of California, Los Angeles, California, 90095, United States
[2]Department of Electrical and Computer Engineering, University of California, Los Angeles, California, 90095, United States
[3]Department of Electrical Engineering, University of California, Berkeley, California, 94720, United States
[4]Department of Electricity and Electronics, University of the Basque Country, Leioa, 48940, Spain
[5]Advanced Light Source (ALS), Lawrence Berkeley National Laboratory, Berkeley, California 94720, United States
[6]Department of Chemical and Biochemical Engineering, University of California, Los Angeles, California, 90095, United States
[7]California Nanotechnology Systems Institute (CNSI), Los Angeles, California, 90095, United States
[8]Department of Mechanical and Aerospace Engineering, University of California, Riverside, California, 92521, United States

E-mail: cslynch@engr.ucr.edu

Received xxxxxx
Accepted for publication xxxxxx
Published xxxxxx

Abstract

This work demonstrates that magnetoelectric composite heterostructures can be designed at the length scale of 10 microns that can be switched from a magnetized state to a vortex state, effectively switching the magnetization off, using electric field induced strain. This was accomplished using thin film magnetoelectric heterostructures of $Fe_{81.4}Ga_{18.6}$ on a single crystal (011) $[Pb(Mg_{1/3}Nb_{2/3})O_3]_{0.68}$-$[PbTiO_3]_{0.32}$ (PMN-32PT) ferroelectric substrate. The heterostructures were tripped from a multi-domain magnetized state to a flux closure vortex state using voltage induced strain in a piezoelectric substrate. FeGa heterostructures were deposited on a Si-substrate for SQUID magnetometry characterization of the magnetic properties. The magnetoelectric coupling of a FeGa continuous film on PMN-32PT was characterized using a MOKE magnetometer with bi-axial strain gauges, and magnetic multi-domain heterostructures were imaged using X-Ray Magnetic Circular Dichroism – Photoemission Electron Microscopy (XMCD-PEEM) during the transition to the vortex state. The domain structures were modelled using MuMax[3], a micromagnetics code, and compared with observations. The results provide considerable insight into designing magnetoelectric heterostructures that can be switched from an "on" state to an "off" state using electric field induced strain.

Keywords: FeGa, Micromagnetics, Magnetostriction, XMCD-PEEM, Piezoelectric, Microstructures, and Modelling

1. Introduction

Magnetoelectric composites enable a variety of applications due to the coupling between magnetization and electric field induced strain [1]. These composites have been explored for magnetic memory [2], antennas [3], and lab-on-chip devices [4]. The integration of these magnetoelectric composites with microfluidic channels has opened the door to new applications in the biomedical and biotechnology fields due to their ability to manipulate magnetic nanoparticles for magnetic activated cell sorting (MACS) systems [5]. This enables future technologies for personalized therapeutics, as well as the isolation/selection of specific stem cells and T-cells for cancer immunotherapies [4,5]. Magnetoelectric composites are scalable down to the micro/nano-scales, energy efficient, and enable local addressability of individual magnetic elements [6-8].

Magnetoelectric composites utilize mechanical coupling between magnetostrictive and piezoelectric materials for electric control of magnetism. A composite that has garnered attention couples $Fe_{81.4}Ga_{18.6}$ (Galfenol) for its large saturation magnetostriction, soft magnetic properties, and high saturation magnetization [9,10] with [011] single crystal $[Pb(Mg_{1/3}Nb_{2/3})O_3]_{(1-x)}$ -$[PbTiO_3]_x$ (PMN-xPT) for its massive piezoelectric coefficient (d_{32}) of 2000 pC/N [11]. FeGa is cost effective, oxidation resistant, machinable, and has advantageous mechanical properties [12]. Several groups have deposited high quality FeGa textured thin films using DC magnetron sputtering [12-14]. Switching mechanisms in FeGa nanoscale heterostructures have been explored for memory [15] and dipole-dipole coupled logic devices [16]. However, electric field driven FeGa MACS systems operating in a microfluidic environment are only recently being explored. Fluorescent optical imaging has demonstrated the capturing and control of superparamagnetic (SPM) particles using FeGa square and ring structures [17] and dot-structures ≥ 20 μm [18], but domain structures have not been imaged and particle capture, and release has not yet been demonstrated. These FeGa heterostructures on PMN-PT required non-linear piezo strains > 2000 ppm to induce magnetization rotation of < 40º. These strains are non-deterministic since the phase transition electric field (E_c) is dependent on the pre-stress state, temperature, and composition (x). Therefore, a linear deterministic piezo strain is desirable for inducing significant moment re-orientation (> 40º) or switching magnetic state. Previously, non-deterministic magnetic state switching was demonstrated for Co nano-ellipses in a surface acoustic wave (SAW) device, where a stress wave (≥ 30 MPa) changed the magnetic state from a stable single-domain to a non-volatile vortex state [19]. Complexities of SAW devices include the

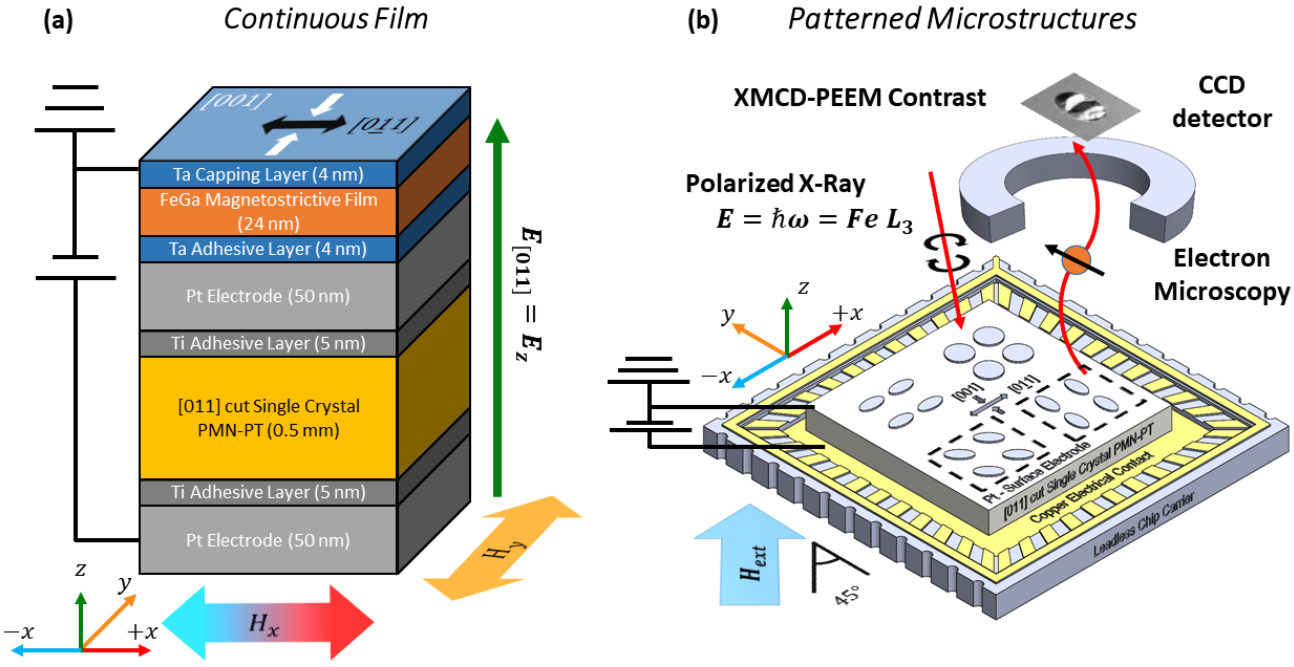

Figure 1: Experimental set-up for thin films deposited on (011) cut single crystal PMN-32PT. (a) Schematic for the continuous thin films' characterization. The crystallographic orientations of the PMN-32PT, [001] (white), [01$\underline{1}$] (black), and [011] (green), are aligned parallel to the "y" (orange), "x" (red and blue) and "z" (green) axes of the reference coordinate system (bottom left), respectively. The external magnetic fields H_x and H_y were applied, along [01$\underline{1}$] and [001] directions, respectively. (b) Schematic showing the patterned microstructures' characterization using XMCD-PEEM, with the same the crystallographic orientation and coordinate system. In (a) and (b) an external electric field is applied along the [011] crystallographic direction to induce an anisotropic in-plane strain in the magnetostrictive film.

creation of strain waves throughout the structures, additional steps during the fabrication process, and difficulty in actuating specific elements [5,20].

In this work a method to trigger magnetic state switching from a metastable multi-domain to a vortex state in FeGa heterostructures using electric field is presented. *In-situ* electric field X-Ray Magnetic Circular Dichroism – Photoemission Electron Microscopy (XMCD-PEEM) imaging was conducted in FeGa micro-ellipses to observe the evolution from a multi-domain state to a vortex state. The remanent magnetization in the initial multi-domain state was characterized using a Superconducting Quantum Interference Device (SQUID) magnetometer. Magnetoelectric response was characterized using a Magneto Optical Kerr Effect (MOKE) magnetometer and bi-axial strain gauges. The experimental results were combined with computational modelling to provide new insight into the development of FeGa-based magnetoelectric devices.

2. Experimental Set-Up

Three magnetic heterostructure configurations were fabricated and characterized: (1) continuous FeGa film on PMN-32PT, (2) patterned FeGa microscale heterostructures on PMN-32PT, and (3) patterned FeGa microscale heterostructures on a Si-substrate.

2.1. Continuous Film

2.1.1. Specimen Preparation

The continuous FeGa film on PMN-32PT was used to quantify the piezoelectric and magnetoelectric responses. The continuous film FeGa shown in Figure 1 (a) consisted of Ta(4 nm)/FeGa(24 nm)/Ta(4 nm) multi-layers grown by DC magnetron sputtering on top of a ferroelectric (011) cut single crystal PMN-32PT procured from Atom Optics. Continuous thin film electrodes of Pt(50 nm)/Ti(5 nm) nm were evaporated on the top and bottom surfaces of the PMN-32PT (10x10x0.5 mm3). The substrate was poled by applying an electric field of 0.8 MV/m through the thickness of the substrate prior to deposition. The FeGa layer was deposited on the grounded side of the substrate using a ULVAC JSP-8000 DC magnetron sputtering system with a base pressure of 2x10-7 Torr, DC sputtering power of 200 W, Ar working pressure of 0.5 mTorr and an FeGa target with atomic ratio of 85:15 for elements Fe and Ga. Is speculated that these films are to be texture, since sputtered deposited FeGa is known to growth in columns [13]. Tantalum films were deposited on both sides of the FeGa film as barrier and capping layers.

2.1.2. Characterization Methods

The continuous film was characterized using (1) a MOKE magnetometer with *in-situ* electric field, and (2) a bi-axial strain gauge interfaced with a National Instrument Data Acquisition (NI-DAQ). The MOKE measurements were conducted at an electric field of 0 and 0.8 MV/m to observe changes in magnetic hysteresis due to the induced ferroelectric strains from the PMN-32PT. The magnetic fields H_y and H_x were applied along the in-plane crystallographic orientations [001] and [0$\underline{1}$1] of the PMN-32PT, respectively. The principal in-plane strains along [001] and [0$\underline{1}$1] were characterized using axial strain gauges. Two sets of strain measurements were conducted by driving the electric field from 0 to 0.8 MV/m to observe non-linear response associated with a phase transformation, and from 0 to 0.4 MV/m to observe the linear piezoelectric response [21]. All measurements were conducted at room temperature [12,21].

2.2. Patterned Microstructures

2.2.1. Specimens Preparation

The FeGa structures on PMN-32PT shown in Figure 1 (b) were produced using photolithography with the same layer profile as shown in Figure 1 (a). The ellipse sizes were 10 μm major diameter, aspect ratio of ~1.5, and thickness of 24 nm. In the lithography step, the structures were patterned using a chromium UV mask, negative photoresist nLoF-2020 and AZ300-MiR developer. The lift-off process was carried out in an ultrasonic bath with stripper NMP (1-methyl-2-pyrrolidone) for 30 minutes to remove the remaining photoresist. Afterwards, the electric bias (bottom) side of the patterned PMN-32PT substrate was adhered to a leadless chip carrier (LCC) using double sided conductive copper tape to assure electrical conductivity. The patterned surface (top side) of the PMN-32PT was wire bonded to the ground terminal pins of the LCC to enable electrical connection during characterization. Similar size FeGa ellipses were fabricated on a (6x6x0.5 mm^3) Si-substrate.

2.2.2. Characterization Methods

The patterned structures were characterized using XMCD-PEEM at the beamline 11.0.1 located at the Advanced Light Source (ALS), Lawrence Berkeley National Laboratory. The structures were magnetically initialized in-plane at $\mu_0 H_{ext} = 200mT$ to induce a remanent magnetization; and prior to imaging, an Ar ion milling process was used to remove the top Ta capping layer and clean the top surface just prior to loading the specimen into the beamline end-station. The external magnetic field (H_{ext}) shown in Figure 1(b) was applied at 45º with respect to the in-plane piezoelectric principal strain components for deterministic domain rotation [18,22]. The Fe-L_3 absorption edge (~708.3 eV) signal was used to maximize the contrast in the magnetic domain images. The images were collected with a field-of-view (FoV) of 45μm, capturing all four structures in the (2x2) array. Scans were conducted prior to applying an *in-situ* electric field to observe the multi-domain structures in the micro-ellipses. Images were

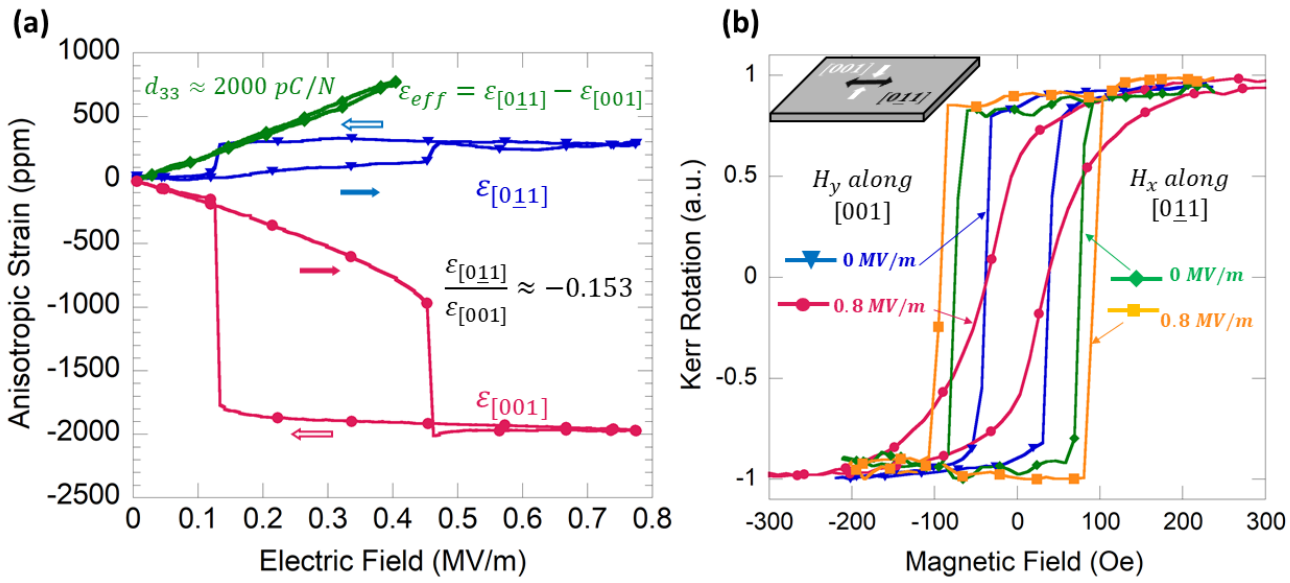

Figure 2: Results of the characterization in the continuous films magnetoelectric device. (a) Characterization of the PMN-32PT anisotropic in-plane strains using two axial strain gauges. Solid and hollow arrows (for blue and red curves) are the directions of the increasing and decreasing electric field, respectively. The green curve is the linear piezoelectric response. (b) Characterization of the FeGa film using MOKE with in-situ electric field. The "blue" and "red" curves are the measurements of the magnetic field H_y parallel to the compressive [001] direction (white). The "green" and "orange" curves are the measurements of the magnetic field H_x parallel to the tensile [0$\underline{1}$1] direction (black).

retaken at 0.2 MV/m electric field increments to observe the magnetic domain structure evolution. An image processing scheme was developed for the structures shown in Figure 1(b) at 0 MV/m to quantify their normalized remanent magnetization. The FeGa structures on a Si-substrate were used to quantify the average magnetization. The micro-ellipses on the Si-substrate were characterized using a SQUID. These measurements were performed along two different directions, at 45° relative to the ellipse long axis and parallel to the short axis.

3. Results

3.1. Magnetoelectric Characterization

3.1.1. Strain Gauge Measurements

Figure 2 (a) shows the PMN-32PT strain versus electric field in the linear piezoelectric region ("green") and the non-linear region where an electric field driven phase transformation takes place ("red" and "blue"). The ferroelectric response is linear at increasing electric fields (solid arrows) up to 0.45 MV/m. The PMN-32PT goes through a phase transition at $E_c \approx 0.45\ MV/m$ from rhombohedral to orthorhombic, yielding a jump in the strains $\varepsilon_{[0\underline{1}1]}$ and $\varepsilon_{[001]}$ along both crystallographic [0$\underline{1}$1] and [001] directions. In the orthorhombic phase ($E > 0.45\ MV/m$) the polarization rotates to the [011] direction, producing the maximum in-plane strain. The maximum compressive strain component ($\varepsilon_{[001]}$) is larger than the tensile strain component ($\varepsilon_{[0\underline{1}1]}$) with an anisotropic in-plane strain ratio of ~0.153. As the electric field is decreased (hollow arrows), a second jump in the strain occurs at an electric field of ~0.15 MV/m, as the reverse phase transformation from orthorhombic to rhombohedral occurs [21,23-25]. In the second electric field cycle from 0 to 0.4 MV/m (green curve), the piezo strain difference ($\Delta\varepsilon = \varepsilon_{[0\underline{1}1]} - \varepsilon_{[001]}$) is close to linear and does not display the jumps associated with the phase transformation. In the linear response regime, the piezoelectric coefficient was measured as $d_{32} \approx 2000\ pC/N$ and the piezo strain difference was $\Delta\varepsilon \approx 800\ ppm$ at 0.4 MV/m.

3.1.2. MOKE Measurements

Figure 2 (b) shows the MOKE measured normalized magnetization (e.g., $m = M/M_s$) response of the FeGa continuous film on the PMN-32PT substrate along the compressive [001] and tensile [0$\underline{1}$1] axes. The magnetoelastic easy and hard axis orientations were determined by the changes in the coercive fields and shape of the hysteresis loops. Prior to applying an electric field, the magnetic coercive fields along the compressive [001] ("blue") and tensile [0$\underline{1}$1] ("green") axes were ~42.6 and ~76.2 Oe, respectively. The coercive field difference along these two axes is attributed to anisotropic residual stress associated with the PMN-32PT remanent strain. Averaging these magnetic coercivities yields 59.4 Oe, close to the magnitude reported for bulk FeGa (~50 Oe) [12]. The opposite shift of the coercive field from the average values is due to the opposite strains felt from both directions. A remanent magnetization (m_r) of ~0.8 was

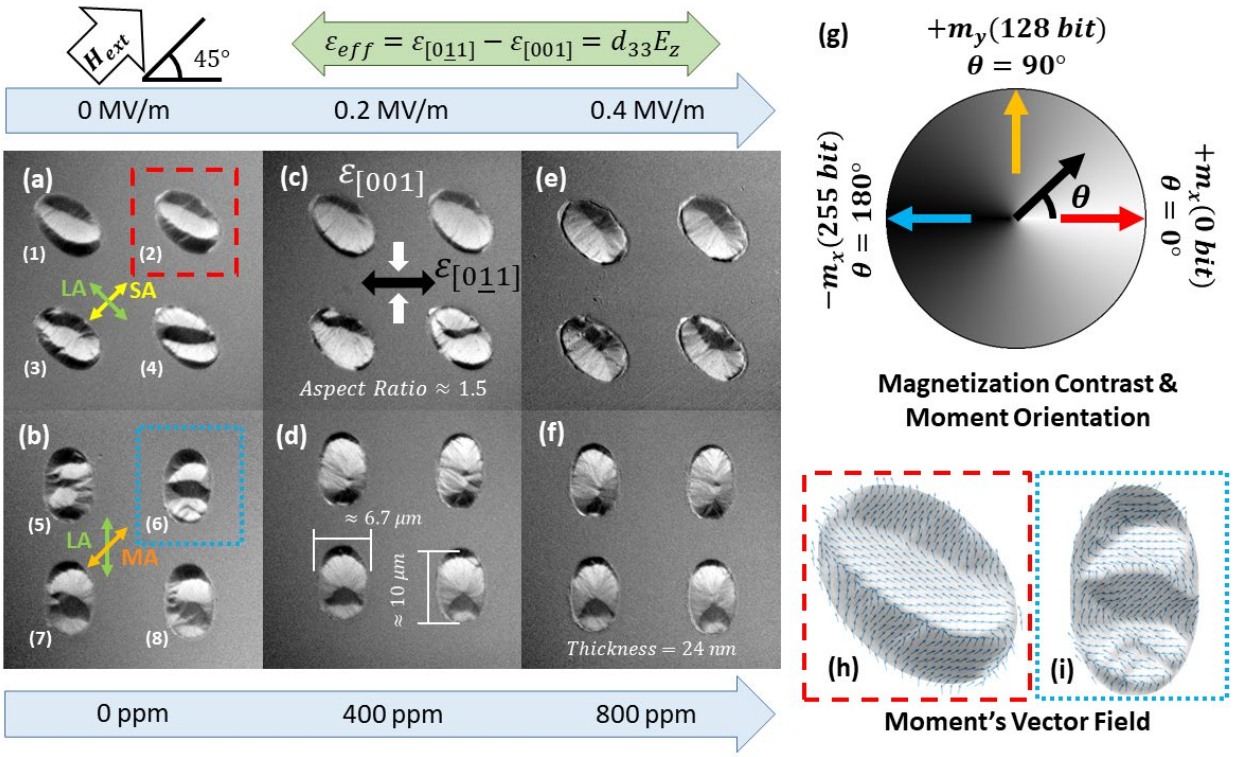

Figure 3: XMCD-PEEM results for the FeGa microstructures. Initial magnetic domains state of microstructures oriented at (a) 45º and (b) 90º. Green, yellow, and orange axes are the orientations of the ellipses long (LA), short (SA) and middle (MA) axes, respectively. (c) and (d) Magnetic domains states at electric field of 0.2 MV/m. (e) and (f) Magnetic domains states at electric field of 0.4 MV/m. Bottom blue arrow correspond to the magnitude of the linear piezo strain difference. Top green axis is the orientation of the piezo strain difference. Top left arrow is the initial direction of the applied magnetic field. (g) Legend for magnetization contrast (m_x). The orientations of the red (+ x), orange (+ y), and blue (- x) arrows are the reference coordinate system. (h) and (i) Are the moments vector field ($\underline{m}$) from the red dashed and blue dotted squares insets in (a) and (b), respectively.

observed along [001] and [0$\underline{1}$1]. Upon application of E=0.8 MV/m, the piezo strains induce (e.g., $\varepsilon_{[0\underline{1}1]}$ and $\varepsilon_{[001]}$) a magnetoelastic easy and hard axis were induced along the tensile [0$\underline{1}$1] and compressive [001] axes, respectively. The anisotropic magnetostriction coefficients $\lambda_{[100]}$ and $\lambda_{[111]}$ for FeGa are both positive [26], therefore the magnetization rotates toward the tensile [0$\underline{1}$1] axis, resulting in this being the easy axis. The magnetoelastic easy axis along the [0$\underline{1}$1] orientation ("orange") increases the coercivity up to ~93.4 Oe. This response is desirable since the [0$\underline{1}$1] axis should be the favourable direction of magnetization. The magnetoelastic response along the compressive [001] direction changes the hysteresis curve ("red") producing a relatively harder magnetoelastic axis. Along the [001] hard axis the magnetic field to saturate the film (H_s) increased from ~70 to ~200 Oe, whereas the remanent magnetization dropped from ~0.8 ("blue") to ~0.6 ("red"). A reduction in the coercivity of 2 Oe is observed. The changes in saturation field and remanent magnetization were anticipated given the positive magnetostriction.

3.2. XMCD-PEEM Imaging

3.2.1. XMCD-PEEM with In-situ Electric Field

These magnetoelastic easy and hard axes were induced in the micro-ellipse heterostructures to observe the evolution of the magnetic domains in response to the linear piezoelectric strain. Figure 3 shows the magnetic domains in the FeGa structures prior to and during application of the *in-situ* electric field in the XMCD-PEEM. In Figure 3 (a-b), prior to applying the electric field, the heterostructures were magnetized parallel to the short axis (SA) and middle axis (MA) of the ellipses, respectively. In Figure 3 (a) the heterostructures displayed "S" shape multi-domain with a net magnetization along the SA. In Figure 3 (b) the heterostructures display a "Zig zag" shaped multi-domain with a net magnetization along the long axis (LA), this 45º re-orientation is due to the shape anisotropy easy axis In Figure 3 (c) with $E = 0.2\ MV/m$ a piezo-strain of 400 ppm (green ε_{eff}) is induced along the "x" axis (red/blue arrows), inducing changes in the domain structure. In Figure 3 (d) the tensile ε_{eff} was parallel to the shape anisotropy hard axis, resulting in a vortex state [17,22,27,28]. In Figure 3 (e) with $E = 0.4\ MV/m$, the piezo strain difference ($\Delta\varepsilon$) of 800 ppm cause a switching into the vortex state. In Figure 3 (f) no significant change was observed compared to 3(d) since these structures had already reached the vortex state. The evolution of the magnetic domains (Figure 3 (a) to (e)) demonstrates that magnetic state

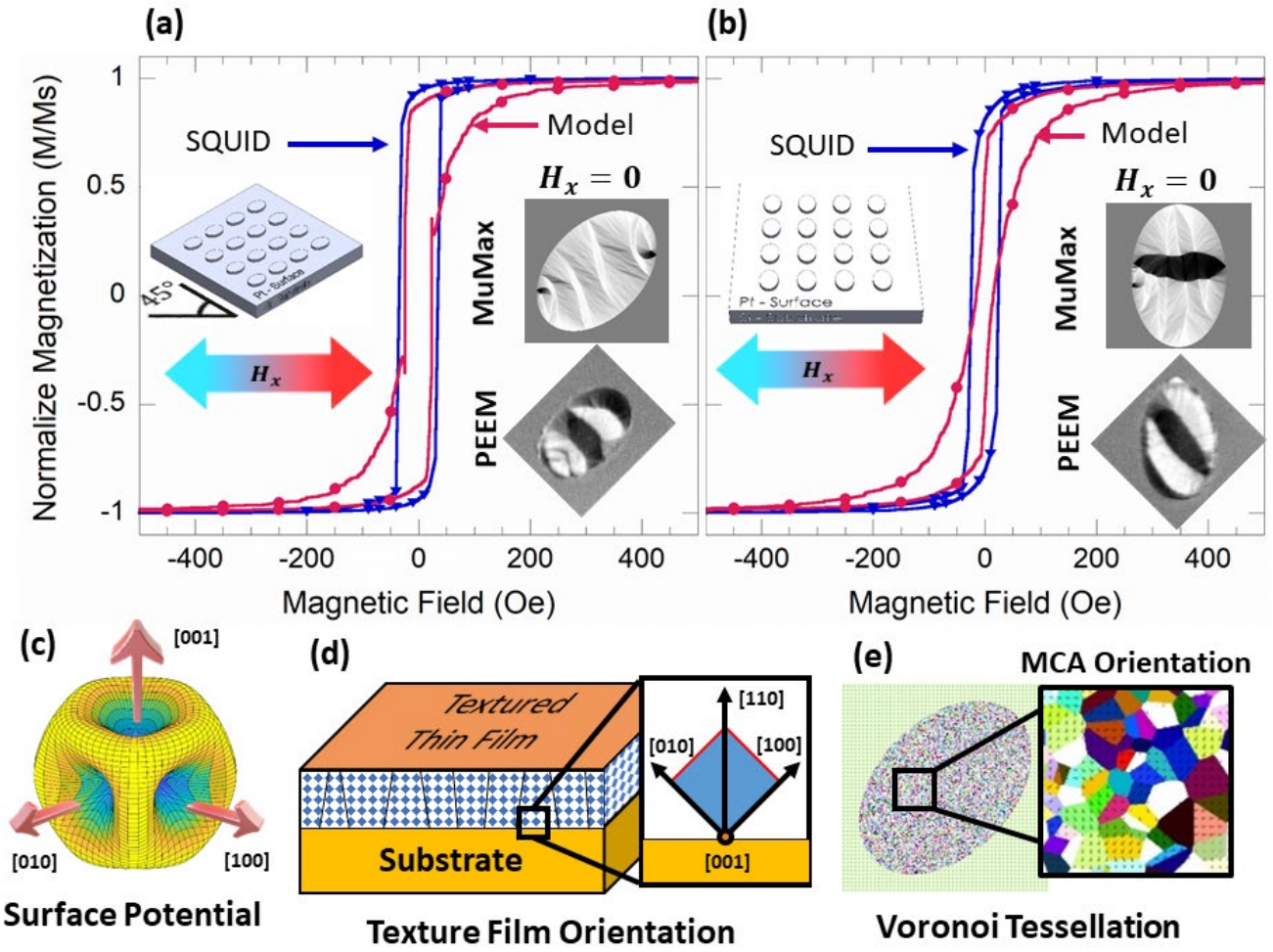

Figure 4: Micro-ellipses SQUID characterization on the Si-substrate and MuMax[3] modelling. (a) Magnetization response along the MA of the microstructures. (b) Magnetization response along the SA of the microstructures. In (a) and (b), "blue" and "red" lines are the SQUID and MuMax3 results, respectively. Left insets in (a) and (b) are the Si-substrate orientation to the external magnetic field. Right inset in (a) and (b) are the snapshots of the multi-domains from the model moment component m_x (top) and XMCD-PEEM imaging (bottom) rotated 45º clockwise. (c) MCA surface potential for FeGa. "Red" arrows are the <100> crystallographic orientations and magnetocrystalline anisotropy easy axes. (d) Columnar profile in FeGa textured polycrystal thin film. Zoom-in, [110] OOP crystallography orientation of FeGa. The crystallographic orientation [001] arrow is pointing out-of-page. (e) Voronoi tessellation used to model texture polycrystal thin films. Zoom-in, each colour represents a unique [001] crystallographic/MCA in-plane orientation.

switching from the multi-domain state to the vortex state can be driven using the linear piezoelectric strain. The vortex state persisted after removal of the electric field because the micro-ellipses require an external magnetic field for re-magnetization [19]. Variations between the domain structures in Figure 3 (a-f) is noticeable. These variations are attributed to local imperfections. An image processing scheme was conducted to quantify the remanent magnetization and its variations.

3.2.2. Image Contrast Processing

The variations observed in the multi-domains in Figure 3 (a-b) are attributed to material imperfections, fabrication anomalies, and randomness of the spin dynamics [19,29]. An image contrast processing scheme was developed to quantify the remanent magnetization (m_r) from these multi-domains. Figure 3 (g) shows the conversion scale ($180°/255bit$) used to translate the magnetic moment contrast ($\pm m_x$ and $+m_y$) into moment orientation (θ). This conversion is only valid for $m_y > 0$ and $m_z \approx 0$. It is assumed that the multi-domain in Figure 3 (a-b) satisfy these conditions. This analysis was not implemented to the vortex state from Figure 3 (c-f) since there no net magnetization (*e.g.*, $m_r = 0$). After converting every pixel (0 to 255 bits) within the micro-ellipses to moment angles (θ) the moments components $m_x = cos\theta$ and $m_y = sin\theta$ were calculated and plotted. Figure 3 (h) and (i) are the computed moment vector fields resembling the "S" and "Zig zag" multi-domain states. These multi-domain configurations illustrate ~90º rotations between adjacent domains as expected from soft-ferromagnetic 90º domain-walls (DWs) for a material such as FeGa.(29) Equation (1) and (2) were used to calculate the average magnetization components $m_{x,avg}$ and $m_{y,avg}$. The values from equation (1) and (2) were used to

approximate the remanent magnetization (m_r) using equation (3), with the results given in Table 1. Collectively the m_r values for the microstructures in Figure 3 (a) were lower than those of the microstructures in Figure 3 (b). The lower m_r values from the microstructures in Figure 3 (a) were due to magnetization alignment with SA, since the magnetic moments do not favor the shape anisotropy "hard" axis. The higher values of m_r for the structures in Figure 3 (b) were attributed to the magnetization being oriented along MA, which favours the shape anisotropy "middle" axis. Despite the standard deviation (S. D.) shown in Table 1, the influence of the shape anisotropy is evident.

$$m_{x,avg} = \frac{1}{N_p}\sum_{p=1}^{N_p} m_x \quad (1)$$

$$m_{y,avg} = \frac{1}{N_p}\sum_{p=1}^{N_p} m_y \quad (2)$$

$$m_r \approx \sqrt{m_{x,avg}^2 + m_{y,avg}^2} \quad (3)$$

Figure 3 (a)					
(1)	(2)	(3)	(4)	AVG	S. D.
0.579	0.576	0.666	0.682	0.626	0.049
Figure 3 (b)					
(5)	(6)	(7)	(8)	AVG	S. D.
0.696	0.640	0.743	0.736	0.704	0.041

Table 1: Remanent Magnetization.

3.3. SQUID Characterization

The original magnetization direction (*e.g.,* along SA and MA) affected the switching behaviour, therefore characterization of the micro-ellipses along these directions is required. Figure 4 (a) and (b) show SQUID magnetization measurements (blue curve) along the "middle" (MA) and "short" (SA) axis, respectively, for the micro-ellipses on the Si-substrate. Figure 4 (a) indicates a remanent magnetization (m_r) of ~0.94 and coercivity (H_c) of ~ 45 Oe along the MA. In Figure 4 (b) the remanent magnetization (m_r) is ~0.81 and coercivity (H_c) is ~ 25 Oe along the SA. These remanence values were compared to the multi-domains in Figure 3 (a-b).

The remanent magnetization acquire from the SQUID characterization were ~0.94 and ~0.81 for the middle and short axis of the micro-ellipses on the Si-substrate (Figure 4). This difference is attributed to (1) the roughness of the PMN-32PT surface relative to the Si- substrate and (2) to the accuracy of the image processing scheme. Surface roughness (R_a) in Si-substrates and PMN-32PT are < 1 and ≥ 5 nm, respectively. Rougher surfaces (R_a > 5 nm) are more susceptible to magnetic pinning sites. The accuracy of the image processing is limited by the number of structures, magnetic contrast images available, and quality/resolution of the images. The SQUID data is a collective average response from thousands of micro-ellipses on the Si-substrate, while the results in Table 1 are limited to the four ellipses for each of the "S" and "Zig zag" configurations.

Modelling of a micro-ellipse was conducted to further understand the remanent magnetization and coercivity from the SQUID, and the multi-domain observed in the XMCD-PEEM images.

3.4. Micromagnetic Modelling

3.4.1. Modelling Crystallinity

Modelling the magnetic domain Figure 3 (a-b) included the effects of long- and local-range magnetic moments. Shape anisotropy is a long-range effect. The films and heterostructures were polycrystalline with local intergranular interactions that include magnetocrystalline anisotropy (MCA) and magnetoelastic anisotropic. These intergranular effects contribute to the formation and evolution of the magnetic domains. In un-constrained ($\underline{\underline{\sigma}} = 0$) highly magnetostrictive materials, the MCA, elastic and magnetoelastic behaviour are coupled, causing a modulation in the effective 2nd order MCA ($K_{c1}^{eff} = K_{c1} + \Delta K$).(29) This modulation $\Delta K = (9/4)\left[(C_{11} - C_{12})\lambda_{[100]}^2 - C_{44}\lambda_{[111]}^2\right]$ occurs in single crystals.(30) Bulk single crystal magnetostrictive $Fe_{81.4}Ga_{18.6}$ ($\lambda_{[100]} = \left(\frac{2}{3}\right)395\ ppm$) has been reported [31] to be BCC quasi-cubic, with 2nd order $K_{c1} = 35kJ/m^3$ proportional to the 4th order $K_{c2} = -9K_{c1}/4$, indicating that the <100> are the MCA easy axes, and the <110> and <111> axes are equally hard. Figure 4 (c) shows the modulated MCA surface potential for magnetostrictive single crystal BCC FeGa, where the depth of the wells are the <100> easy axes, and the height of the ridges are the equally hard <110> and <111> axes. The nano-crystallite grains share the same cubic symmetry conditions as their bulk counterpart, therefore the modulation of the 2nd order (K_{c1}^{eff}) and the proportionality of the 4th order ($K_{c2}^{eff} = -9K_{c1}^{eff}/4$) must be considered for each grain in the textured polycrystal film. The orientation of the cubic nano-crystallite axes (*e.g.,* <100>, <110>, and <111>) are impacted by the dominant grain orientation from the growth process. For instance, sputter-deposited FeGa films with columnar growth reported in the literature were textured films with a (110) out-of-plane (OOP) crystallographic orientation as shown in Figure 4 (d) with an average column diameter (*i.e.,* Grain Size, GS) of ~40 nm [13]. The zoom-in image of Figure 4 (d) shows the easy axes orientations [100] and [010] at 45° from the OOP direction,

and the [001] in the in-plane orientation (out of page). As shown, the [001] easy axis will be the preferred easy axis due to the in-plane shape anisotropy, but it is a localized interaction that changes as a function of the grain profile (*e.g.,* GS, geometry, distribution, and random in-plane [001] orientation). Figure 4 (e) shows a 2D Voronoi tessellation that resembles the grain profile observed in texture thin films. The zoom-in image of Figure 4 (e) shows the microscopic random in-plane orientations of the [001] easy axis, where the magnetic moments within each grain were assigned a unique MCA orientation associated with the grain orientation.(32) The formation of the multi-domain structures in the modelling approach included a coupling response from the long range (> 1 um) interactions of the shape anisotropy, and short range intergranular interactions (GS ~ 40 nm) of the MCA. The 2nd order modulation and the 4th order proportionality are necessary to model the multi-domains seen in Figure 3 (a-b). The MCA modulation ΔK in this model were derived on the assumption that this an un-constrained system $\underline{\underline{\sigma}} = 0$, therefore uniaxial anisotropy K_{u1} representing magnetoelastic interaction cannot be implemented [29].

3.4.2. Model Parameters

The multi-domain structures were modelled using the finite difference (FD) micromagnetic solver MuMax[3]. It has the capability to integrate and couple these different anisotropic fields (long range and local interactions) [33]. The same ellipse dimensions (diameter, aspect ratio, and thickness) as in the experiments (XMCD-PEEM and SQUID) were used to capture the effect of shape anisotropy. Local nano-crystal interactions were modelled using a built-in 2D Voronoi tessellation function. A FD grid with element length of 6 nm. The magnetic and elastic properties for FeGa used in the calculations are provided in Table 2, *i.e.* exchange constant (A_{ex}), Gilbert damping coefficient (α), magnetic saturation (M_s), 1st order MCA constant (K_{c1}), and the anisotropic magnetostriction coefficients $\lambda_{[100]}$ and $\lambda_{[111]}$, and the stiffness coefficients are C_{11}, C_{12}, and C_{44}. The computational study consisted of sweeping an external magnetic field (H_x) ±500 Oe under ramp function of 1 Oe/ns. Two studies were conducted with H_x along the MA and SA, top-right insets in Figure 4 (a) and (b) respectively.

$A_{ex}(pJ/m)$	14
α	0.06
$M_s(emu/cc)$	1300
$K_{c1}(kJ/m^3)$	35
$\lambda_{[100]}(ppm)$	263.3
$\lambda_{[111]}(ppm)$	13.3
$C_{11}(GPa)$	195
$C_{12}(GPa)$	155
$C_{44}(GPa)$	120

Table 2: FeGa Properties.

3.4.3. Model Results

Figure 4 (a) and (b) show the modelled magnetization response (red curves) along the MA and SA of the micro-ellipse, respectively. The remanent magnetization (m_r) values were approximately 0.88 and 0.52 with respect to MA and SA. The magnetization along MA yielded a higher remanence relative to SA due to the shape anisotropy. These trends are consistent with the results from the XMCD-PEEM images and the SQUID measurements. The modelled coercivity (H_c) values are ~ 24.5 and 15 Oe with respect to MA and SA. The coercivity (H_c) along MA is higher than SA due to shape anisotropy. The top-right inset in Figure 4 (a-b) shows similar "Zig zag" and "S" shape multi-domain to those experimentally observed in the bottom insets of Figure 4 (a-b) from the XMCD-PEEM. The results from Figure 4 (a-b) suggest the multi-domain are caused by the local MCA, film texturing, shape anisotropy, and initial magnetization direction. The model captures the formation of these multi-domains but modelling the switching mechanism require a bi-coupling between micromagnetic and elastodynamics, therefore a fully bi-coupled FEA model is incorporated.

3.5. Finite Element Modelling

3.5.1 Theory

A finite element analysis (FEA) framework is used to model the constrained magnetoelastic system that integrates the micromagnetics phenomenological Landau-Lifshitz-Gilbert (LLG) equation, magnetostatics, and governing equations of elasticity through coupled partial differential equations. This multi-physics system provides a bi-coupled response seen in highly magnetostrictive materials.(34,35)

Evolution of the magnetic moments were modelled using equation (4), the LLG equation,

$$\frac{\partial \underline{m}}{\partial t} = -\mu_0 \gamma \left(\underline{m} \times \underline{H}_{eff} \right) + \alpha \left(\underline{m} \times \frac{\partial \underline{m}}{\partial t} \right) \quad (4)$$

where $\underline{m}$ is the magnetic moment, μ_0 permeability of free space, γ gyromagnetic ratio, and $\underline{H}_{eff}$ is the effective magnetic field. The effective field $\underline{H}_{eff}$ equation (5) is an overall interaction from different magnetic anisotropies,

$$\underline{H}_{eff} = \underline{H}_{ex} + \underline{H}_{mca} + \underline{H}_{ext} + \underline{H}_{d} + \underline{H}_{me} \quad (5)$$

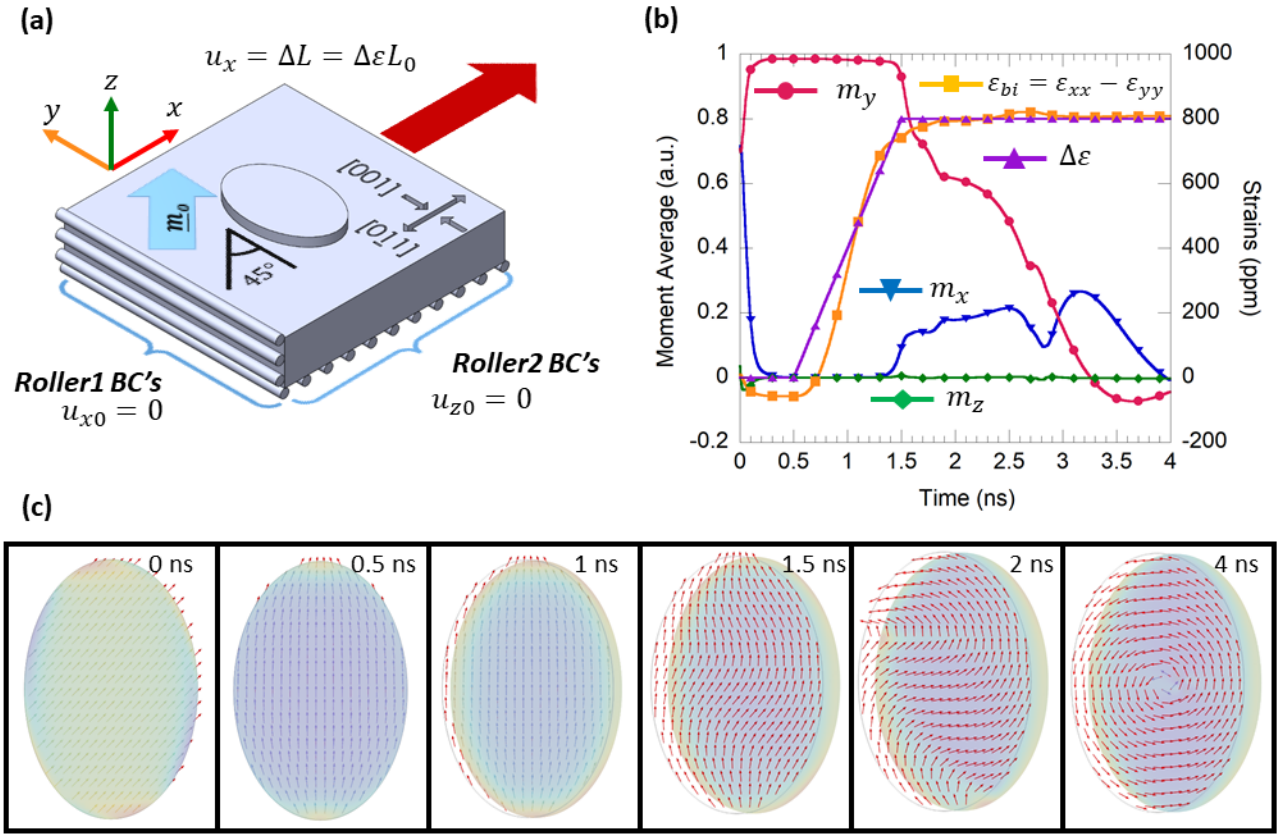

Figure 5: Bi-coupled model set-up and results, following the same reference coordinate system. (a) Geometrical set-up with initial moment orientation ($\underline{m}_0$) and mechanical boundaries ($\underline{u}$) conditions. (b) Time evolution of moment average components (left), and the bi-axial and piezo strain difference (right) response. (c) Snapshots of magnetic moments (red arrows) and displacement/deformation of nanostructures at given time.

where, $\underline{H}_{ex}$ is the exchange field, $\underline{H}_d$ the demagnetization field, $\underline{H}_{mca}$ the magnetocrystalline field, $\underline{H}_{ext}$ the externally applied field, and $\underline{H}_{me}$ the magnetoelastic field. The demagnetization field $\underline{H}_d = -\nabla\varphi$ is the magnetostatic long-range moment interaction induced by the geometry of the microstructure, which was calculated using equation (6),

$$\nabla^2\varphi = -M_s\underline{m}\cdot\hat{n} \quad (6)$$

where φ is the magnetostatic scalar potential, and $\hat{n}$ is the surface normal. The magnetoelastic field components were calculated using equation (7),

$$\begin{bmatrix} H_{me,x} \\ H_{me,y} \\ H_{me,z} \end{bmatrix} = -\frac{1}{\mu_0 M_s}\begin{bmatrix} 2B_1 m_x\varepsilon_{xx} + B_2\left(m_y\varepsilon_{xy} + m_z\varepsilon_{xz}\right) \\ 2B_1 m_y\varepsilon_{yy} + B_2\left(m_x\varepsilon_{xy} + m_z\varepsilon_{yz}\right) \\ 2B_1 m_z\varepsilon_{zz} + B_2\left(m_x\varepsilon_{xz} + m_y\varepsilon_{yz}\right) \end{bmatrix} \quad (7)$$

where B_1 and B_2 are the magnetoelastic coefficients, ε_{xx}, ε_{yy}, and ε_{zz} are the normal strain components, and ε_{xy}, ε_{xz} and ε_{yz} are shear strain components, which are dependent on the elastic and magnetoelastic strain, equation (8),

$$\underline{\underline{\varepsilon}} = \underline{\underline{\varepsilon}}^{el} + \underline{\underline{\varepsilon}}^{me} \quad (8)$$

where $\underline{\underline{\varepsilon}}^{el}$ and $\underline{\underline{\varepsilon}}^{me}$ are the elastic and magnetoelastic strains, respectively. The magnetoelastic strains were calculated using equation (9),

$$\varepsilon_{ij}^{me} = \begin{cases} \frac{3}{2}\lambda_{[100]}\left(m_i m_j - \frac{1}{3}\right) & i = j \\ \frac{3}{2}\lambda_{[111]} m_i m_j & i \neq j \end{cases} \quad (9)$$

the elastic strains are calculated using the governing equation of elasticity and its constitutive relations. The elastic field is assumed to be in an equilibrium state, therefore $\nabla\cdot\underline{\underline{\sigma}} = 0$. The constitutive relation $\underline{\underline{\sigma}} = \underline{\underline{\underline{C}}} : \underline{\underline{\varepsilon}}^{el}$ and the total strain/displacement relation $\underline{\underline{\varepsilon}} = \frac{1}{2}\left(\nabla\underline{u} + \left(\nabla\underline{u}\right)^T\right)$ are coupled to the magnetic field using equation (8); the equilibrium equation is re-written as equation (10),

$$\nabla \cdot \underline{\underline{\underline{C}}} : \left[\frac{1}{2} \left(\nabla \underline{u} + \left(\nabla \underline{u} \right)^T \right) \right] - \nabla \cdot \underline{\underline{\underline{C}}} : \underline{\underline{\varepsilon}}^{me} = 0 \qquad (10)$$

where $\underline{u}$ is the displacement field. Equations (4), (6) and (10) are solved using a weak formulation in COMSOL Multi-Physics package [35].

3.5.2. FEA Results

Figure 5 (a) shows the geometry of the model. A 300x200x24 nm^3 nano-ellipse was placed on top of a uniform elastic substrate. An elastic substrate was used to impose a strain through the nanostructure. The strain was generated by implementing roller boundary conditions at the left (u_{x0}) and bottom(u_{z0}) side of the substrate, and a displacement on the right (u_x) side of the substrate. The displacement (u_x) was set to produce the linear piezoelectric strain difference ($\Delta\varepsilon$). The displacement was ramped linearly at a rate of 800 ppm/ns. Once the maximum $\Delta\varepsilon$ of 800 ppm was reached, the displacement (u_x) was held fixed to observe the magnetic moment evolution under the imposed magnetoelastic easy axis. The initial direction of the magnetic moments ($\underline{m}_0$) was at 45º from the "x" axis along the nano-ellipse middle axis. Figure 5 (b) and (c) show the average responses of the magnetic moment components, prior to and during the application of $\Delta\varepsilon$ inducing a magnetoelastic easy axis along the "*x*" direction. Initially, at 0 ns, the moments are uniformly aligned in-plane at 45º from the "*x*" and "*y*" axes (*e.g.*, the ellipse middle axis); after relaxation of 0.5 ns the moments re-aligned themselves along the ellipse long axis. The re-orientation of the moments is due to the shape anisotropy induced easy axis. In addition, a single domain was observed due to the scale of the nano-ellipse where local- exchange interactions dominate over long-range demagnetization effects; therefore, no meta-stable multi-domain configuration is observed. This implies that nanoscale structures are not as sensitive of the initial magnetization direction as its microscale counterpart, therefore meta-stable multi-domain cannot be achieved in a nano-ellipses. Prior to applying $\Delta\varepsilon$, a magnetostrictive strain $\underline{\underline{\varepsilon}}^{me}$ was observed from the 45º rotation of the single domain, since the bi-axial strain ($\varepsilon_{bi} = \varepsilon_{xx} - \varepsilon_{yy}$) was compressive. When ramping up $\Delta\varepsilon$ in the substrate, the strain was transferred into the nano-ellipse elastic strain $\underline{\underline{\varepsilon}}^{el}$ resulting in an increase of ε_{bi} in the "*x*" direction. At the maximum strain ($\Delta\varepsilon = 800ppm$), the magnetoelastic easy axis along the shape anisotropy hard axis, caused the magnetic moment to be re-oriented. From 1.5 to 4 ns the magnetic moment component m_y started to collapse, and m_x increased slightly to ~0.2. At the final stage of 4 ns, the magnetic moments transformed into a lower vortex state. During the transition of the magnetic domain state, ε_{bi} converges into $\Delta\varepsilon$, which implies that the average $\underline{\underline{\varepsilon}}^{me}$ in a vortex state is negligible, and only the average $\underline{\underline{\varepsilon}}^{el}$ is observed (~800 ppm). In comparison to the structures from the XMCD-PEEM results (Figure 3 (b) and (d)) where 400 ppm was needed for the magnetic state switching, the nano-ellipse requires double $\Delta\varepsilon$. The difference in magnitude of $\Delta\varepsilon$ was due to the difference between a stable single-domain and a meta-stable multi-domain configuration. The multi-domain "S" and "Zig-Zag" configurations (Figure 3 (a-b)) can rotate incoherently, whereas the single domain configuration rotates coherently. To capture the multi-domain configurations a larger structure would have to be modelled, but this is not possible with the constraint that elements size must be smaller than the domain wall width. The results of Figure 5 indicate that the bi-coupled model is a practical tool to model and design new strain-mediated multiferroics. The bi-coupled model has been validated on a Ni system [35]. This model was tested for Terfenol-D [34] and FeGa [36] but such systems has not been develop, therefore lacking validation. The results presented here are first validation for FeGa system.

4. Discussion

This work is the first to demonstrate that magnetoelectric composite heterostructures can be designed at the length scale of 10 microns that can be switched from a magnetized state to a vortex state using electric field induced strain. Earlier work [19] had shown that single-domain nano-ellipses could be tripped to a vortex state, but this effect only occurred in a small fraction of the ellipses in sub-micron structures. The experiments presented here take advantage of the shape anisotropy of the ellipse shape that gives an easy axis along the MA and a hard axis along the SA. This was seemed through the remanence (m_r) and coercive field (H_c) values of the MA being relatively higher to the SA. This was used together with a magnetostriction induced easy and hard axis associated with a bi-axial strain state produced by a [011] PMN-32PT substrate (tensile and compressive in-plane strain components). Initial modelling work using MuMax without the single crystal properties of FeGa did not produce the observed "S" and "Zigzag" domain structures. This led to consideration of the effects of grain structure in the textured film. Once the grain structure was added and the anisotropic elastic and magnetostriction included, the model produced the observed domain structures. This modelling approach should now work well for the design optimization of other shaped structures on the 10's of micron scale. The interaction of the shape anisotropy with the strain induced magnetostriction was shown to trip the magnetization from a metastable multi-domain configuration to a non-volatile vortex configuration. This behaviour cannot not be captured by the MuMax model. The energetics of the single-domain state and the vortex state were investigated using the FEA model.

This FEA model is limited to nanoscale structures but did demonstrate the switching between the stable single-domain

state and the non-volatile vortex state, providing an assessment of the relative energy levels between the two states. Due to the nanoscale of the ellipse exchange interaction was dominant over long-range demagnetization interactions. The influence of the shape anisotropy was still noticeable, since $\underline{m}_0$ was initially at 45º from the shape anisotropy easy axis, therefore causing re-orientation of the single domain. Similar re-orientation was seen in micro-ellipses in Figure 3 (b), but the demagnetization interaction was dominant, therefore causing a non-coherent rotation of the multi-domains. The vortex state configuration was found to be at a global minimum in the energy landscape. The vortex state is stable and non-volatile, meaning that it does not switch back to its original configuration upon removal of the electric field [19].

5. Conclusion

In conclusion, piezoelectric strains were used to induce a magnetoelastic response in magnetostrictive continuous and patterned FeGa films. Magnetoelastic coupling was strongly correlated to the magnetostriction (λ_s) and piezoelectric (d_{32}) coefficients from the FeGa and PMN-32PT, respectively. In the micro-ellipses the piezo strain in conjunction with the shape anisotropy, converted the metastable multi-domain configurations into a vortex state, where switching was achieved using linear strains ≤ 800 ppm. The multi-domain configurations were a direct consequence of the size and geometry of the micro-ellipses, the initial magnetization direction, and the granular structures of the texture FeGa thin film, as indicate by the SQUID characterization and the FD modelling. This ability to switch off the magnetization in magnetoelectric composite heterostructures on the 10's micron length scale is anticipated to be useful in biomedical and biotechnology applications where cells tagged with magnetic particles can be captured by the remanent magnetization (> 0.5 M_s) and released upon localized application of electric field [17,18,22]. This quasi-static electric field driven magnetic state switching can be exploited in the design of multiferroic composites with localized electrodes where non-linear strains > 2000 ppm or electric fields > 0.4 MV/m are not available [7,8,37].

Acknowledgements

This work was supported by the National Science Foundation (NSF) Engineering Research Center (ERC) for Translational Applications of Nanoscale Multiferroic Systems (TANMS) under the Cooperative Agreement Award (EEC-1160504). The work at the Advanced Light Source, Lawrence Berkeley National Laboratory (XMCD-PEEM at beamline 11.0.1.1) is supported by the Director, Office of Science, Office of Basic Energy Science, the U.S. Department of Energy, under contract number DE-AC02-05CH11231. The authors acknowledge the use of the fabrication facility at the Integrated Systems Nanofabrication Cleanroom (ISNC) of the California NanoSystems Institute (CNSI), and the UCLA NanoLab. Magnetic data was acquired on a SQUID supported by the NSF MRI-1625776, and the MOKE System in Prof. Kang Wang Device Research Laboratory, UCLA. Author M.G.J. acknowledges the TANMS and Cota Robles fellowships. Finally, we acknowledge the insightful discussions with Dr. Andres Chavez, Auni Kundu, Kevin Fitzell, and Scott Keller.

References

[1] Ryu J, Priya S, Vázquez Carazo A, Uchino K, Kim HE. Effect of the Magnetostrictive Layer on Magnetoelectric Properties in Lead Zirconate Titanate/Terfenol-D Laminate Composites. J Am Ceram Soc. 2001;84(3–12):2905–8.

[2] Roy A, Gupta R, Garg A. Multiferroic memories. Adv Condens Matter Phys. 2012;2012.

[3] Yao Z, Wang YE, Keller S, Carman GP. Bulk Acoustic Wave-Mediated Multiferroic Antennas: Architecture and Performance Bound. IEEE Trans Antennas Propag. 2015;63(8):3335–44.

[4] Wyatt Shields Iv C, Reyes CD, López GP. Microfluidic cell sorting: A review of the advances in the separation of cells from debulking to rare cell isolation. Lab Chip. 2015;15(5):1230–49.

[5] Lee W, Tseng P, Di D, Editors C. Microsystems and Nanosystems Microtechnology for Cell Manipulation and Sorting. New York: Springer; 2017.

[6] Eerenstein W, Mathur ND, Scott JF. Multiferroic and magnetoelectric materials. Vol. 442, Nature. 2006. p. 759–65.

[7] Cui J, Hockel JL, Nordeen PK, Pisani DM, Liang CY, Carman GP, et al. A method to control magnetism in individual strain-mediated magnetoelectric islands. Appl Phys Lett. 2013;103(23):232905.

[8] Cui J, Liang CY, Paisley EA, Sepulveda A, Ihlefeld JF, Carman GP, et al. Generation of localized strain in a thin film piezoelectric to control individual magnetoelectric heterostructures. Appl Phys Lett. 2015;107(9):0–5.

[9] Clark AE. Magnetic and Magnetoelastic Properties of Highly Magnetostrictive Rare Earth-Iron Laves Phase Compounds. 1974;1015(1974):1015–29.

[10] Cullen JR, Clark AE, Wun-Fogle M, Restorff JB, Lograsso TA. Magnetoelasticity of Fe-Ga and Fe-Al alloys. J Magn Magn Mater. 2001 May 1;226–230(PART I):948–9.

[11] Park S-E, Shrout TR. Ultrahigh strain and piezoelectric behavior in relaxor based ferroelectric single crystals. J Appl Phys. 1998 Jun 4;82(4):1804.

[12] Atulasimha J, Flatau AB. A review of magnetostrictive iron-gallium alloys. Vol. 20, Smart Materials and Structures. IOP Publishing; 2011. p. 043001.

[13] Acosta A, Fitzell K, Schneider JD, Dong C, Yao Z, Sheil R, et al. Underlayer effect on the soft magnetic, high frequency, and magnetostrictive properties of FeGa thin films. J Appl Phys. 2020 Jul 7;128(1):13903.

[14] Gopman DB, Sampath V, Ahmad H, Bandyopadhyay S, Atulasimha J. Static and Dynamic Magnetic Properties of

Sputtered Fe-Ga Thin Films. IEEE Trans Magn. 2017 Nov 1;53(11).
[15] Ahmad H, Atulasimha J, Bandyopadhyay S. Reversible strain-induced magnetization switching in FeGa nanomagnets: Pathway to a rewritable, non-volatile, non-toggle, extremely low energy straintronic memory. Sci Rep. 2015;5(December):1–7.
[16] Ahmad H, Atulasimha J, Bandyopadhyay S. Electric field control of magnetic states in isolated and dipole-coupled FeGa nanomagnets delineated on a PMN-PT substrate. Nanotechnology. 2015 Sep 16;26(40).
[17] Xiao Z, Khojah R, Chooljian M, Conte R Lo, Schneider JD, Fitzell K, et al. Cytocompatible magnetostrictive microstructures for nano- A nd microparticle manipulation on linear strain response piezoelectrics. Multifunct Mater. 2018;1(1):0–10.
[18] Khojah R, Xiao Z, Panduranga MK, Bogumil M, Wang Y, Goiriena-Goikoetxea M, et al. Single-Domain Multiferroic Array-Addressable Terfenol-D (SMArT) Micromagnets for Programmable Single-Cell Capture and Release. Adv Mater. 2021;2006651:2006651.
[19] Sampath V, D'Souza N, Bhattacharya D, M. Atkinson G, Bandyopadhyay S, Atulasimha J. Acoustic-Wave-Induced Magnetization Switching of Magnetostrictive Nanomagnets from Single-Domain to Nonvolatile Vortex States. Nano Lett. 2016 Aug 31;16(9):5681–7.
[20] Gedge M, Hill M. Acoustofluidics 17: Theory and applications of surface acoustic wave devices for particle manipulation.
[21] Gallagher JA, Tian J, Lynch CS. Composition dependence of field induced phase transformations in [0 1 1]C PIN-PMN-PT relaxor ferroelectric single crystals with d322 piezoelectric mode. Acta Mater. 2014 Dec 1;81:512–23.
[22] Sohn H, Nowakowski ME, Liang CY, Hockel JL, Wetzlar K, Keller S, et al. Electrically driven magnetic domain wall rotation in multiferroic heterostructures to manipulate suspended on-chip magnetic particles. ACS Nano. 2015;9(5):4814–26.
[23] Lv P, Lynch CS. Energetics of domain engineered rhombohedral ferroelectric single crystals. Behav Mech Multifunct Mater Compos 2017. 2017;10165(April 2017):101650B.
[24] Lv P, Lynch CS. Phase-field simulation of domain walls in rhombohedral ferroelectric single crystals. Acta Mater. 2018;155:245–52.
[25] Lv P, Wang L, Lynch CS. A phenomenological thermodynamic energy function for PIN-PMN-PT relaxor ferroelectric single crystals. Acta Mater. 2017;137:93–102.
[26] Clark AE, Hathaway KB, Wun-Fogle M, Restorff JB, Lograsso TA, Keppens VM, et al. Extraordinary magnetoelasticity and lattice softening in bcc Fe-Ga alloys. In: Journal of Applied Physics. American Institute of PhysicsAIP; 2003. p. 8621–3.
[27] Xiao Z, Lo Conte R, Goiriena-Goikoetxea M, Chopdekar R V., Lambert CHA, Li X, et al. Tunable Magnetoelastic Effects in Voltage-Controlled Exchange-Coupled Composite Multiferroic Microstructures. ACS Appl Mater Interfaces. 2020 Feb 5;12(5):6752–60.
[28] Lo Conte R, Xiao Z, Chen C, Stan C V., Gorchon J, El-Ghazaly A, et al. Influence of Nonuniform Micron-Scale Strain Distributions on the Electrical Reorientation of Magnetic Microstructures in a Composite Multiferroic Heterostructure. Nano Lett. 2018;18(3):1952–61.
[29] O'Handley R (Massachuttes I of T. Modern Magnetic Materials, Principles and Applications. Physics Bulletin. John Wiley & Sons, Inc; 2000.
[30] Wohlfarth EP. Handbook of Ferromagnetic Materials Vol 1,. 1988;632.
[31] Rafique S, Cullen JR, Wuttig M, Cui J. Magnetic anisotropy of FeGa alloys. In: Journal of Applied Physics. American Institute of PhysicsAIP; 2004. p. 6939–41.
[32] Al Misba W, Rajib M, Bhattacharya D, Atulasimha J. Acoustic-Wave-Induced Ferromagnetic-Resonance-Assisted Spin-Torque Switching of Perpendicular Magnetic Tunnel Junctions with Anisotropy Variation. Phys Rev Appl. 2020;10:14088.
[33] Vansteenkiste A, Leliaert J, Dvornik M, Helsen M, Garcia-Sanchez F, Van Waeyenberge B. The design and verification of MuMax3. AIP Adv. 2014;4(10).
[34] Xiao Z, Lo Conte R, Chen C, Liang CY, Sepulveda A, Bokor J, et al. Bi-directional coupling in strain-mediated multiferroic heterostructures with magnetic domains and domain wall motion. Sci Rep. 2018;8(1):1–10.
[35] Liang CY, Keller SM, Sepulveda AE, Bur A, Sun WY, Wetzlar K, et al. Modeling of magnetoelastic nanostructures with a fully coupled mechanical-micromagnetic model. Nanotechnology. 2014;25(43).
[36] Chen C, Sablik J, Domann J, Dyro R, Hu J, Mehta S, et al. Voltage manipulation of magnetic particles using multiferroics. J Phys D Appl Phys. 2020 Apr 22;53(17).
[37] Xiao Z, Lai C, Zheng R, Goiriena-Goikoetxea M, Tamura N, Juarez CT, et al. Localized strain profile in surface electrode array for programmable composite multiferroic devices. Appl Phys Lett. 2021 May 3;118(18).